A positivity-preserving scheme for the aircraft icing droplet equations within SU2

Thomas Vigier, Héloïse Beaugendre, François Morency

Proceedings of the 29th Annual Conference of the Computational Fluid Dynamics Society of Canada
CFDSC2021
July 27-29, 2021, Online

A positivity-preserving scheme for the aircraft icing droplet equations within SU2

Thomas Vigier[1], Héloïse Beaugendre[2] and François Morency[3]

[1] *INRIA, University of Bordeaux, CNRS, Bordeaux INP, IMB, UMR 5251, F-33400 Talence, France*
[2] *University of Bordeaux, INRIA, CNRS, Bordeaux INP, IMB, UMR 5251, F-33400 Talence, France*
[3] *Mechanical Engineering Department, Ecole de technologie supérieure, Montréal, Canada*

Email: *thomas.vigier@inria.fr*

1 INTRODUCTION

Icing effect is one of the main concerns for aircraft security and constitutes a very active research field. In clouds and under cold weather conditions, droplets impact the aerodynamic structure. Impinging droplets can solidify or create a thin liquid film depending on ambient temperature and other flow characteristics. Therefore, ice may accumulate on the wing and induce a lift reduction and a drag increase. As a consequence, the stall angle is lowered and the general performance is degraded [2].

Ice accretions are still responsible for many crashes and accidents [1]. Predicting the droplets impingement is the first step to better anticipate in-flight icing and to design ice protection devices. Physically, the air flow around the wing transports suspended water droplets and, because of their high inertia, they impact along the aircraft surface instead of getting around the obstacle [3]. In the literature, two approaches have been developed to model the droplets impact; the Lagrangian one who track the particles in their individual motion and the Eulerian one who describes the droplets continuously as a density (or volume fraction of water) and a velocity field.

In this work, the Eulerian approach is chosen. The objective of this study, is to extend the capabilities of the open-source SU2 CFD software [4] to 3D aircraft icing using the Eulerian droplet model formulation to solve the droplet impingement [5]. The architecture of SU2, solving PDE systems, suits well for the implementation of the Eulerian droplet model. In this paper, the main purpose is to implement a numerically stable finite volume scheme for the Eulerian formulation of the droplet equations. The resulting method should preserve physical properties such as the density positivity and must produce accurate results compared to existing codes (NASA Lewice [10], FENSAP-ICE Drop3d [3]). The model equations and the numerical method will first be presented before demonstrating the 3D capabilities in the results section, with comparisons and verification against results from the literature.

2 EULERIAN DROPLET FORMULATION AND NUMERICAL SCHEME

The Eulerian description of the droplet model involves two variable fields: the droplet velocity ($\mathbf{U}$) and the volume fraction of water (α). The first equation is deducted from the mass conservation and the second one from the momentum conservation with the standard particle derivative.

$$\begin{cases} \dfrac{\partial \alpha}{\partial t} + \nabla \cdot (\alpha \mathbf{U}) = 0 \\ \dfrac{\partial \alpha \mathbf{U}}{\partial t} + \nabla \cdot (\alpha \mathbf{U} \otimes \mathbf{U}) = \mathbf{F}_a + \mathbf{F}_g \end{cases} \tag{1}$$

Gravity, $\mathbf{F}_g$, and air friction, $\mathbf{F}_a$, act on the droplets and take the following dimensional form

$$\mathbf{F}_g = \alpha(1 - \frac{\rho_a}{\rho_w})\mathbf{g} \tag{2a}$$

$$\mathbf{F}_a = \alpha \frac{3\mu_a C Re}{4\rho_w d^2}(\mathbf{U}_a - \mathbf{U}) \tag{2b}$$

where Re is the Reynold number of the droplets in the air flow, $\mathbf{U}_a$ the air velocity, C the experimental drag coefficient, d the average droplet diameter and ρ_a, μ_a, ρ_w the density and viscosity of the air and the water density.

At the wall, special boundary conditions are needed to mimics droplet impact. The impinging droplets are absorbed by

the wall but cannot leave the wall. Slip or noslip wall, or outlet boundary condition are unsuitable on the aircraft solid surface. Consider a droplet with a velocity $\mathbf{U}_b$ that flow on a surface with a normal vector $\mathbf{n}$ positive away from the wall. When the projection of the droplet velocity on the surface is positive, the net flux of the droplet that leave the surface is 0. As a consequence the boundary condition depends of the velocity projection sign to match the physical behaviour:

$$\begin{cases} \alpha\mathbf{U}_b = \mathbf{0} & \text{if } \mathbf{U}\cdot\mathbf{n} \geq 0 \\ \alpha\mathbf{U}_b = \alpha\mathbf{U} & \text{otherwise} \end{cases} \tag{3}$$

The resulting set of equations 1 is close to the Euler equations but without a pressure term. Consequently, the resulting system is not strictly hyperbolic and standard Riemann solvers can not be used. Many approaches have been developed to solve this problem such as using a Jordan decomposition or introducing a small term to artificially restore hyperbolicity [8]. In this study, the adopted approach is to add to the momentum part of the droplet model an isothermal pressure term, αgd, proportional to the volume fraction of water α, and where g is gravity and d the droplet diameter. This term, $\mathbf{F}_n$, is also added to the source term so that the system remains exact [5].

$$\begin{cases} \dfrac{\partial\alpha}{\partial t} + \nabla\cdot(\alpha\mathbf{U}) = 0 \\ \dfrac{\partial\alpha\mathbf{U}}{\partial t} + \nabla\cdot(\alpha\mathbf{U}\otimes\mathbf{U} + \alpha gdI) = \mathbf{F}_a + \mathbf{F}_g + \mathbf{F}_n \end{cases} \tag{4}$$

$$\mathbf{F}_n = \begin{pmatrix} 0 \\ gd\nabla\alpha \end{pmatrix} \tag{5}$$

Near the aircraft surface, in the shadow area, the volume fraction can be close to zero. Unphysical negative volume fraction may easily appears if an appropriate Riemann solver is not used. For example the Roe solver can lead to this problem and high space orders are difficult to achieve [5]. As a consequence, this issue is the main concern to develop positivity-preserving Rieman solvers. The positivity-preserving property is related to the solver capacity at resolving shock and rarefaction waves. The HLLC approximate Riemann solver satisfies this property and shows a good behaviour at solving the intermediate waves [6]. It has consequently been chosen and adapted to this problem by [5].

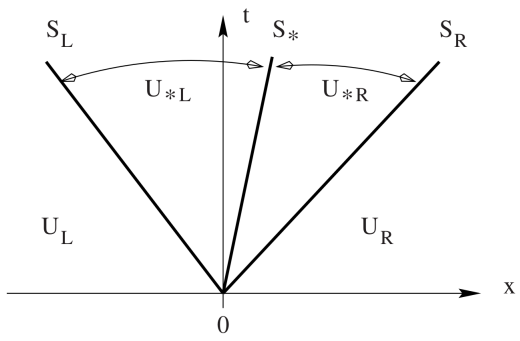

Figure 1: The HLLC Riemann solver

The vector of conservative variables $\mathbf{W} = (\alpha, \alpha\mathbf{U})$ is introduced and the general law of conservation takes the following form with (**F**, **G**, **H**) the flux matrix:

$$\partial_t\mathbf{W} + \partial_x\mathbf{F}(\mathbf{W}) + \partial_y\mathbf{G}(\mathbf{W}) + \partial_z\mathbf{H}(\mathbf{W}) = \mathbf{S} \tag{6}$$

On an interface between two cells, with $\mathbf{n}$ the normal vector and $V = \mathbf{U}\cdot\mathbf{n}$, the transversal flux is:

$$\mathbf{Z}(\mathbf{W}) = (\mathbf{F},\mathbf{G},\mathbf{H})(\mathbf{W})\cdot\mathbf{n} = \begin{pmatrix} \alpha V \\ \alpha V\mathbf{U} + \alpha gd\mathbf{n} \end{pmatrix} \tag{7}$$

The droplet equations satisfy the rotational invariance property like the Euler equations. As a consequence, the solver is constructed from a reduce conservation law and involves rotations to move the problem from the cross direction to the x one. This property greatly simplify the solver construction and involves one or two rotation matrices depending on the problem dimension.

In 3D, the resulting rotation matrix is a combination of a $\mathbf{e}_y$ and $\mathbf{e}_z$ rotation : $T_{yz}(\theta_y,\theta_z) = T_y(\theta_y)T_z(\theta_z)$. In that case, the rotational property stands as:

$$\mathbf{Z}(\mathbf{W}) = {}^tT_{yz}\mathbf{F}(T_{yz}\mathbf{W}) \tag{8}$$

As a consequence, the problem appears as a one dimensional pressureless Euler equation with the passive transport of two quantities in the tangential directions. The multidimensional solver is directly deducted from the 1D one, with the transversal conservative vector $\tilde{\mathbf{W}} = T_{yz}\mathbf{W}$ and a modified flux $\tilde{\mathbf{F}} = {}^tT_{yz}\mathbf{F}$.

The HLLC solver introduces two intermediate states $\mathbf{W}_L$ and $\mathbf{W}_R$ which are delimited by three speeds as shown in figure 1. The left and right speeds S_K are constructed from the maximum and minimum eigenvalues of the Jacobian and the star region wave speed (S^*) derive from Rankine-Hugoniot conditions rearrangement [6].

$$S_L = V_L - q_L\sqrt{gd} \tag{9a}$$

$$S_R = V_R + q_R\sqrt{gd} \tag{9b}$$

$$S^* = \frac{S_L\alpha_R(V_R - S_R) - S_R\alpha_L(V_L - S_L)}{\alpha_R(V_R - S_R) - \alpha_L(V_L - S_L)} \tag{9c}$$

q_K is a modulation term to better resolve shock waves and α^* is the density in the star region and can be expressed with integral relations between each regions.

$$q_K = \begin{cases} \sqrt{\dfrac{\alpha^*}{\alpha_K}} & \text{if } \alpha^* \geq \alpha_K \\ 1 & \text{if } \alpha^* \leq \alpha_K \end{cases} \tag{10a}$$

$$\alpha^* = \frac{\alpha_L + \alpha_R}{2} - (V_R - V_L)\frac{\alpha_L + \alpha_R}{8\sqrt{gd}} \tag{10b}$$

The numerical flux depends of the velocities signs and the intermediate states are taken according to Toro [6].

$$\tilde{\mathbf{F}}(\tilde{\mathbf{W}}_L, \tilde{\mathbf{W}}_R) = \begin{cases} \tilde{\mathbf{F}}(\tilde{\mathbf{W}}_L) & \text{if } 0 \leq S_L \\ \tilde{\mathbf{F}}(\tilde{\mathbf{W}}_L) + S_L(\tilde{\mathbf{W}}_L^* - \tilde{\mathbf{W}}_L) & \text{if } S_L \leq 0 \leq S^* \\ \tilde{\mathbf{F}}(\tilde{\mathbf{W}}_R) + S_R(\tilde{\mathbf{W}}_R^* - \tilde{\mathbf{W}}_R) & \text{if } S^* \leq 0 \leq S_R \\ \tilde{\mathbf{F}}(\tilde{\mathbf{W}}_R) & \text{if } S_R \leq 0 \end{cases} \tag{11}$$

$$\tilde{\mathbf{W}}_K^* = \alpha_K \frac{S_K - V_K}{S_K - S^*} \begin{pmatrix} 1 \\ S_K^* \\ \mathbf{V}_K^t \end{pmatrix} \tag{12}$$

Where $\mathbf{V}_K^t$ is the tangential velocity in the transversal direction.

This expression of the flux involves multiple rotations and, as a consequence, is not numerically optimal. Simple algebraic manipulations give those simpler forms and remove the rotations:

$${}^tT\mathbf{F}(T\mathbf{W}_K) = \begin{pmatrix} \alpha_K V_K \\ \alpha_K V_K \mathbf{U}_K + \alpha_K g d \mathbf{n} \end{pmatrix} \tag{13a}$$

$${}^tT(\tilde{\mathbf{W}}_K^* - T\mathbf{W}_K) = \frac{S^* - V_K}{S_K - S^*}\left(\mathbf{W}_K + \alpha_K(S_K - V_K)\begin{pmatrix} 0 \\ \mathbf{n} \end{pmatrix}\right) \tag{13b}$$

The additional source term is computed at the same time as the flux by considering the volume fraction of water between two cells according to the HLLC numerical flux:

$$\alpha_{RL} = \begin{cases} \alpha_L & \text{if } 0 \leq S_L \\ \alpha_L^* & \text{if } S_L \leq 0 \leq S^* \\ \alpha_R^* & \text{if } S^* \leq 0 \leq S_R \\ \alpha_R & \text{if } S_R \leq 0 \end{cases} \tag{14}$$

For large computational domain and steady solution, explicit schemes are computationally intensive and may show convergence issues for large time step. In order to use larger CFL numbers, implicit schemes are mandatory. The full discrete numerical scheme is, with the implicit Euler time scheme, $\mathbf{W}_K^n$ the average of $\mathbf{W}$ on the cell K at the n-th iteration, $\mathbf{F}_{a,K}^n$ and $\mathbf{F}_{g,K}^n$ the average of $\mathbf{F}_a$ and $\mathbf{F}_g$ and Δt the time step:

$$\begin{aligned} \forall K,\ \mathbf{W}_K^{n+1} = \mathbf{W}_K^n &- \frac{\Delta t}{|K|}\left(-\mathbf{F}_{a,K}^{n+1} - \mathbf{F}_{g,K}^{n+1}\right) \\ &- \frac{\Delta t}{|K|}\left(\sum_{\substack{e\in\partial K \\ e=K\cap L}} |e|\left(\mathbf{Z}_{\mathrm{HLLC}}(\mathbf{W}_K^{n+1}, \mathbf{W}_L^{n+1}) - gd\alpha_{KL}^{n+1}\begin{pmatrix} 0 \\ \mathbf{n} \end{pmatrix}\right)\right) \end{aligned} \tag{15}$$

A non-linear system needs to be solve at each time iteration. The linearized system involves the numerical flux Jacobian wich is almost the original system Jacobian due to the solver structure [7]:

$$J = \begin{pmatrix} 0 & n_x & n_y & n_z \\ -Vu + \alpha g d n_x & V + n_x u & n_y u & n_z u \\ -Vv + \alpha g d n_y & n_x v & V + n_y v & n_z v \\ -Vw + \alpha g d n_z & n_x w & n_y w & V + n_z w \end{pmatrix} \tag{16}$$

Depending on the signs of S_L, S_R and S^*, the correction term $S_K(\tilde{\mathbf{W}}_K^* - \tilde{\mathbf{W}}_K)$ and its Jacobian can be added. This term can be partially or completely neglected in the Jacobians for the sake of simplicity at the cost of a slower convergence rate for steady computations. In this study, the adopted Jacobians for the left and right states are only the system Jacobian computed with either states.

A regular MUSCL (Monotone Upstream Scheme for Conservation Law) extension is possible within SU2 in order to reach a higher than one space convergence order. A standard second order TVD limiter is used to ensure stability [9].

3 RESULTS

3.1 VERIFICATION

The positivity-preserving property is closely related to the solver capabilities at resolving shock and more importantly, rarefaction waves which often occur in low density areas. In order to showcase the solver in those situations, two 1D explicit simulations (only the hyperbolic part of the droplet equations) creating a rarefaction and a shock wave are established and the results are compared to the analytical solutions [5].

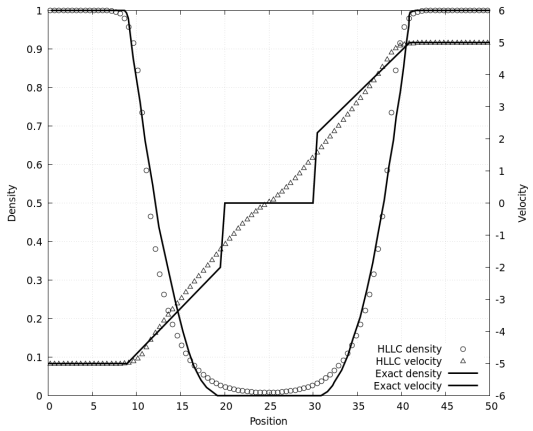

Figure 2: Density and velocity solutions for the 1D rarefaction wave, $g = 9.81$, $d = 0.1m$

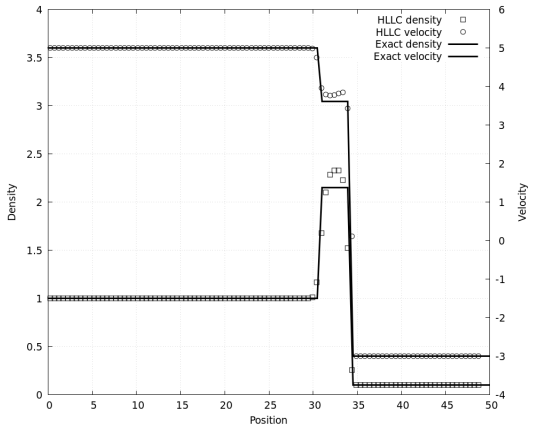

Figure 3: Density and velocity solutions for the 1D shock wave, $g = 9.81$, $d = 0.23m$

Transmissive boundary conditions are taken on both side [9]. As shown, figure 2, the density is accurate (the maximum residue is below 0.1 with 100 points) and remains positive. In the wet region the velocity residue is just as low whereas in the dry region, the zero speed area does not appear. The resolution of shock waves does not present this problem as shown in figure 3. However, the density maximum in the area of the shock is about 15% higher than the exact solution and the velocity 5 % higher with the Van Albada limiter. Overall the shock is overestimated but this issue is really flux limiter dependant. The computed solutions with the same scheme in [5] are similar.

Within SU2, the droplet solution is computed around a NACA 65_2415 cambered airfoil at different angles of attack for an Euler airflow solution with the implicit scheme. As a first approximation, the artificial source term $\mathbf{F}_n$ is disregarded. As a matter of fact, 1D and 2D rarefaction and shock wave tests have shown that its effect is negligible when compared to the physical source terms. Regarding the really specific boundary condition (3), some numerical instability appears in low densities areas where the velocity is also really low. In those cases, to ensure stability, the droplet velocity is approximated by the air velocity. Because of the low density, this approximation has minor to no effect on the collection efficiencies.

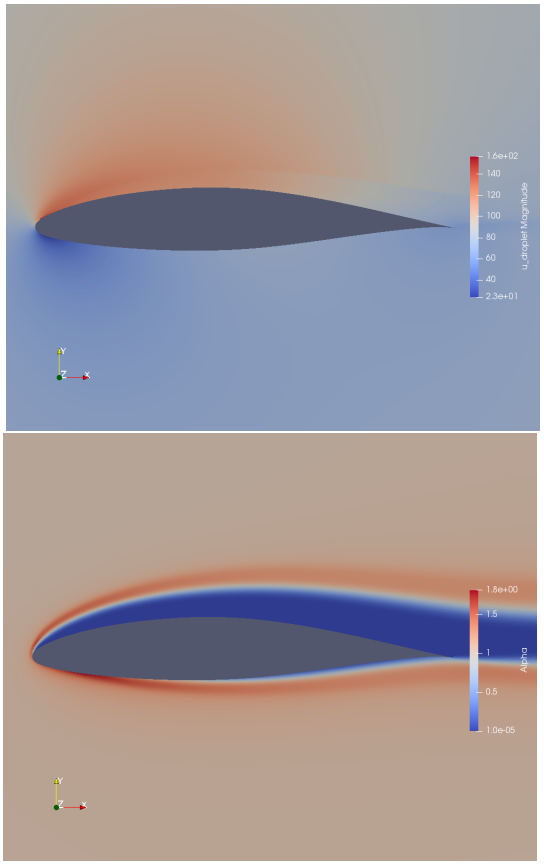

Figure 4: The droplet velocity and volume fraction of water on a NACA 65_2415 airfoil, $d = 21\,\mu m$, Mach=0.23, AoA=8^o, chord=$0.928\,m$

To better understand the scheme behaviour, the density and velocity are represented in figure 4 for the NACA 65_2415 airfoil. The wet and dry regions are clearly visible around the airfoil. On the nose, droplets accumulate and close to the trailing edge a dry region appears. The 1D rarefaction wave test showcases the HLLC difficulties to accurately solve the velocity in low density areas. This behaviour manifests in the region above the upper surface of the airfoil where a non physical discontinuity appears. The highest residuals are concentrated in this area and slow down the convergences on the velocity. The residual is defined as the norm of the difference between to consecutive solutions. Fortunately, those speeds are associated with low densities and as a consequence, are not accompanied with particles transport.

To study the space convergence properties of the scheme, a mesh series is considered for the same airfoil with an approx-

imate element size of $h_n = \dfrac{h_{ref}}{1.4^{n-2}}$ ($n \in [\![1,4]\!]$). The reference element size h_{ref} (for the coarse mesh) is about the size of the chord divided by 200. The local collection efficiency $\beta = \alpha \mathbf{U} \cdot \mathbf{n} / U_\infty$, with U_∞ the air velocity at farfield, is computed around the profile for each meshes. The local collection efficiency represents the droplet impingement intensity on the profile surface and is the quantity of interest in the context of icing.

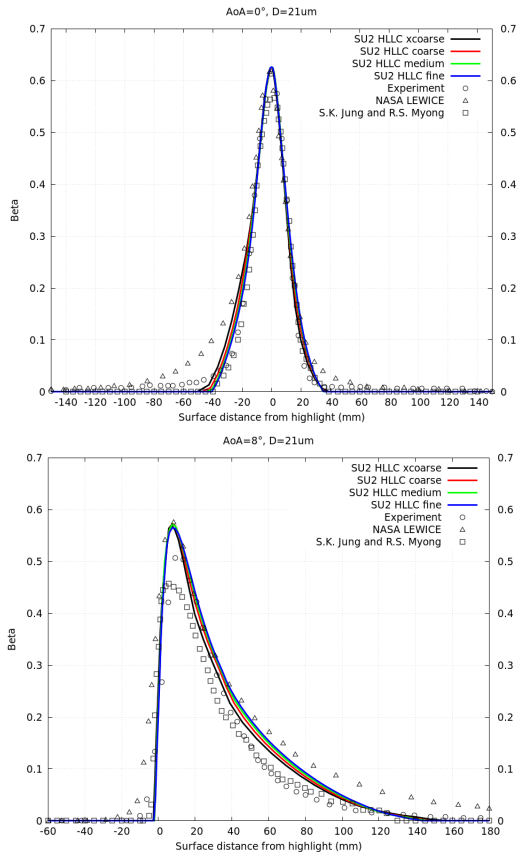

Figure 5: Local collection efficiency sensibility to the mesh size on a NACA 65_2415 airfoil, $d = 21\,\mu m$, Mach=0.23, AoA=0^o and AoA=8^o, chord=$0.928\,m$

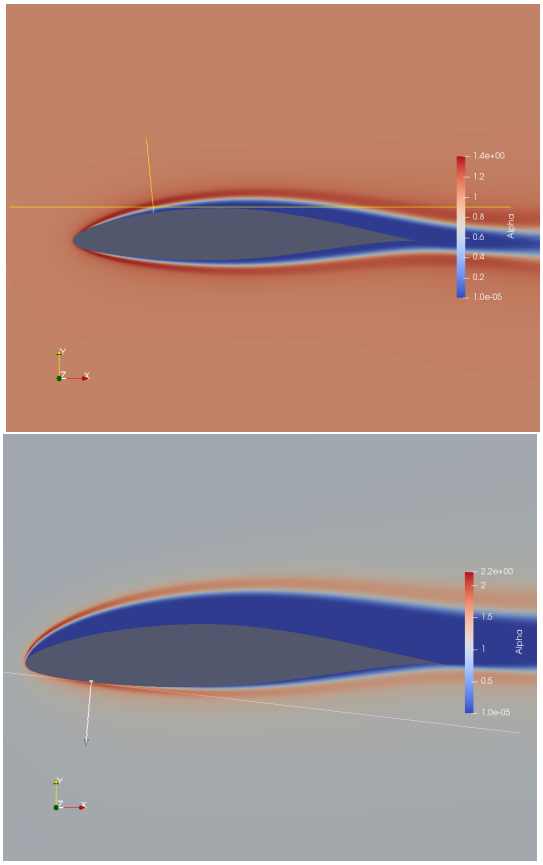

Figure 6: Cutting lines on the NACA 65_2415 airfoil, $d = 21\,\mu m$, Mach=0.23, AoA=0^o and AoA=8^o, chord=$0.928\,m$

Firstly, the maximum remains the same (0.2% between the finest and the coarsest mesh) at both angles. The collection areas are almost identical (0.4%) at 8°, but at 0° a small variation (5%) occurs between the finest and the coarsest mesh. On the lower surface at 8°, the collection efficiency slightly increases with the mesh refinement by 2% at most between each solution. Overall, at both incidence angles, the collection efficiencies are really similar and show only minor variations between each other. This analysis suggests that the collection efficiency is very little sensitive to the mesh size.

In order to study in detail the influence of mesh refinement on the droplet solution, cuts are made on the water volume fraction and velocity fields in normal and tangential directions to the NACA 65_2415 airfoil at two specific positions (figure 6). The first one is on the dry area of the upper surface at 0° and the second one at 8° on the lower surface where the collection efficiency changes the most between meshes as shown in figure 5. Those cuts should show the shock and rarefaction waves between the areas of low and high densities.

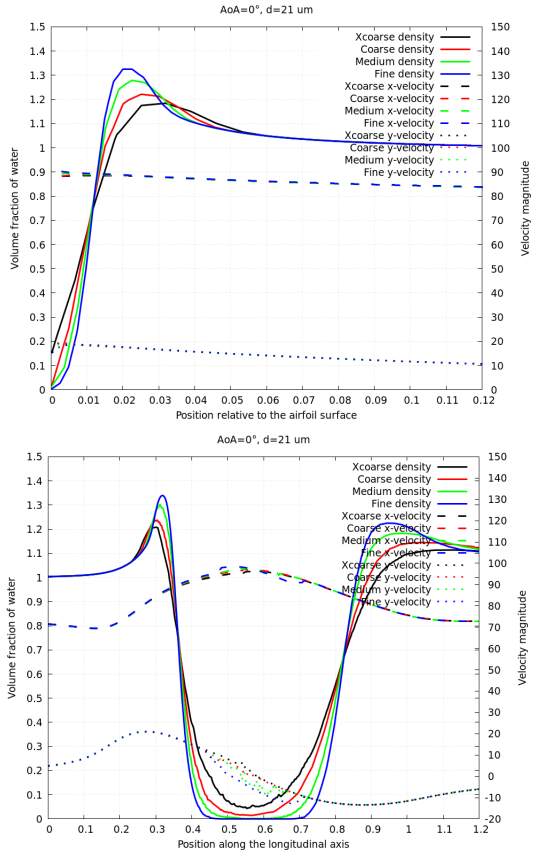

Figure 7: Normal and tangential volume fraction of water and velocity on the NACA 65_2415 airfoil, $d = 21\,\mu m$, Mach=0.23, AoA=0^o, chord=$0.928\,m$

In the first situation, the diffusion of the shock is clearly visible between meshes in both normal and tangential directions. The volume fraction of water maximum dropped by 15 % between the xcoarse and the fine mesh in the normal direction. In the tangential direction, the density decreased according to the element size close to the airfoil surface in the dry area. The density remains positive ($\alpha \geq 10^{-6}$). In both directions, the difference between the velocities doesn't exceed 0.1% except in the tangential one where the fine mesh velocity oscillates in the dry area. The maximum magnitude of those variations is 30% compared to the finest solution. By analogy with the 1D rarefaction test case, the low volume fraction of water creates this minor instability. Because the velocity is not associated with any particle transport in this dry area, the error on the velocity does not impact the volume fraction of water distribution.

The euclidean norm calculation of the difference between the fine mesh volume fraction of water and the other meshes solutions allows to establish the approximate convergence order of the HLLC scheme coupled with a MUSCL extension. The density convergence order is 1.85 in the normal direction and 1.76 in the longitudinal direction. Although this order is smaller than 2, this result was to be expected because the numerical scheme order drop to 1 in the high gradient area and in our case, close to the shock waves.

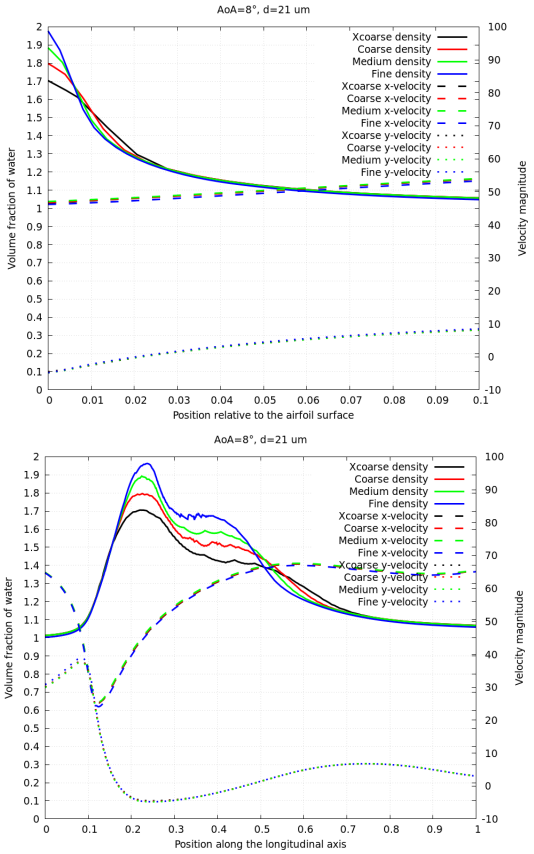

Figure 8: Normal and tangential volume fraction of water and velocity on the NACA 65_2415 airfoil, $d = 21\,\mu m$, Mach=0.23, AoA=$0 = 8^o$, chord=$0.928\,m$

In this second situation, the tangential chart explains the normal volume fraction of water gap close to the airfoil surface. A shock wave appears at this position and, like in the previous example, the shock is diffused in both directions according to the mesh size. The convergence orders are the same at both angle of attack. The good resolution of shock waves on the lower surface is critical to compute an accurate collection efficiency from a numerical point of view. However, the comparisons in the next section show the overall HLLC scheme tendency to compress the density. As a consequence, numerical diffusion does not represent a big issue and a mesh fine enough to resolve the Euler flow solution is enough to solve the droplet equations.

Because the artificial source term is neglected, the artificial pressure term changes the system to restore hyperbolicity. The choice of the d parameter could be different than the droplet diameter and his influence needs to be studied. A tangential cut is used on the same airfoil and the velocity and volume fraction of water are represented on figure 9 for different values of this parameter.

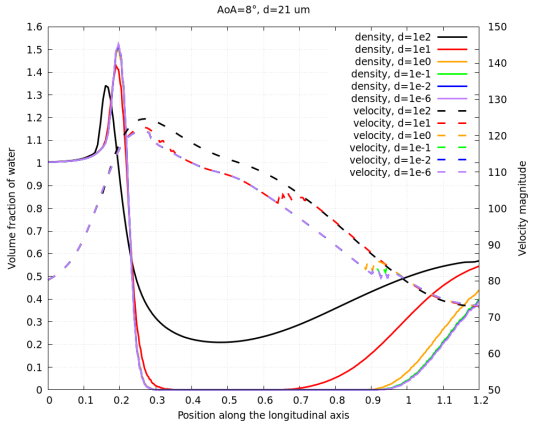

Figure 9: Tangential volume fraction of water and velocity for different stabilisation parameters on the NACA 65_2415 airfoil on the upper surface, $d = 21\,\mu m$, Mach=0.23, AoA=8^o, chord=$0.928\,m$

Both the velocity and the volume fraction of water approach a limit solution when the stabilisation parameter approaches zero. As a consequence, the system limits seem to be the same as the scheme limits. For $d > 10^{-2}m$, the difference norm between the solutions is smaller than 10^{-4}. As a consequence, the stabilisation parameter does not need to be as low as possible and the choice of the real droplet diameter as the stabilisation parameter is usually a good choice to get a good approximation of the limit solution.

3.2 VALIDATION

In this section, the local collection efficiency is compared to other available solutions at a 0° and a 8° incidence angle and with two different droplet diameters (figure 5 and 10). The experimental results are obtained with a complex laser system in a scale model by the NASA [10]. Uncertainties remains mainly because of the difficulty to obtain the desired droplet diameter [10]. Moreover, the LEWICE NASA code uses a Lagrangian approach to compute the droplet impact on the airfoil. The solutions obtained by Jung and Myong [5] are computed with their HLLC scheme but with a Navier-Stokes based air flow.

As shown, figure 5, the maximum collection efficiency is close to LEWICE results but about 5% higher than the experimental maximum at both incidence angles. The Lagrangian code tends to overestimate the captation limits range by almost 50% at 0° and by more than 30% at 8° (on the lower surface). On the contrary, the SU2 HLLC scheme has the tendency to underestimate the range by 30% at 0° and by less than 5% at 8°. Overall, the SU2 HLLC scheme tends to overestimate the collection efficiency and to underestimate the collection area. At both angles, the maximum collection efficiency of the other HLLC solution (by [5]) is 7% lower than the experimental one. However, the collection range is similar (0.01% gap) than the Euler based solution. Overall, the Eulerian approach produces closer results to the experiment than the Lagrangian one in those particular cases. Finally, the use of a Navier-Stokes based air flow seems to lead to an overall underestimation of the local collection efficiency according to Jung and Myong results [5].

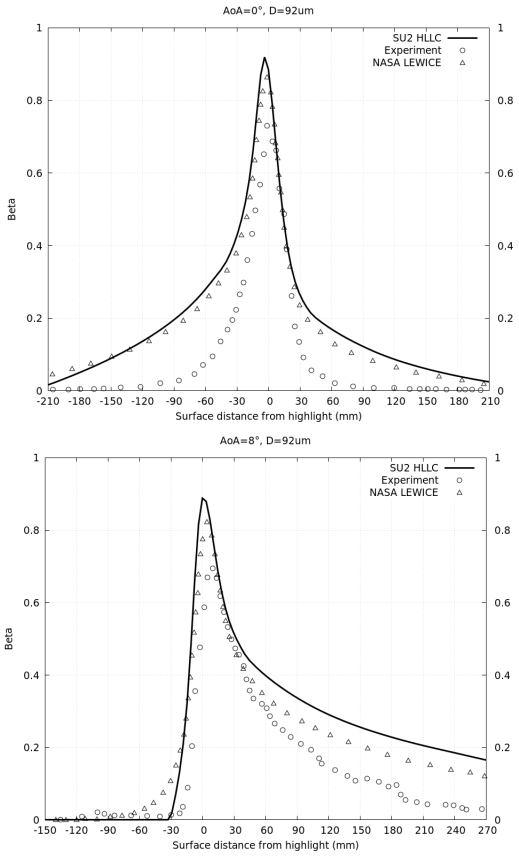

Figure 10: Local collection efficiency on a NACA 65_2415 airfoil, $d = 92\,\mu m$, Mach=0.23, AoA=0^o and AoA=8^o, chord=$0.928\,m$

With a $d = 92\,\mu m$ droplet diameter (figure 10), the previously described behaviour is exacerbated. At both angles, in the maximum collection efficiency areas, both computed solutions are almost confounded and predict the same maximum which is about 15% higher than the experimental one. Outside of this area, at 0°, the collection efficiency is much bigger than expected and the collection range is approximately twice as big. At 8°, on the upper surface the HLLC scheme result is closer to the experimental collection efficiency than the LEWICE code. However, outside of the maximum area, on the lower surface, the Eulerian approach clearly overestimates the collection range as for the other incidence angle. In this situation, the HLLC scheme predicts a collection efficiency 10% higher than Lewice.

Finally, the obtained local collection efficiency is compared for the NACA 0012 airfoil at a 4° incidence angle (figure 11).

The Drop3D code is part of FENSAP-ICE suite and also uses an Eulerian formulation.

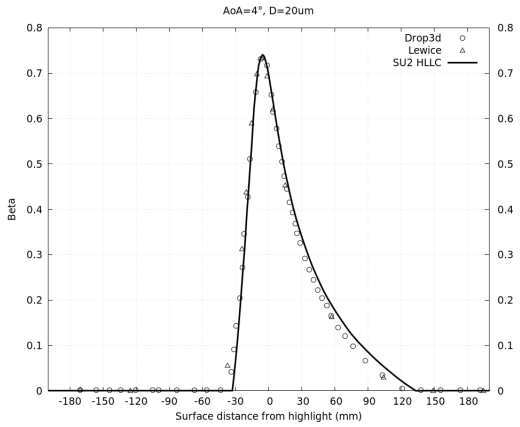

Figure 11: Local collection efficiency around a NACA 0012 airfoil, $d = 20\mu m$, Mach=0.485, AoA=4^o, chord=$0.928\,m$

The solution obtained is mostly in agreement with literature results. On the lower surface, the HLLC scheme overestimates the collection efficiency compared to other codes.

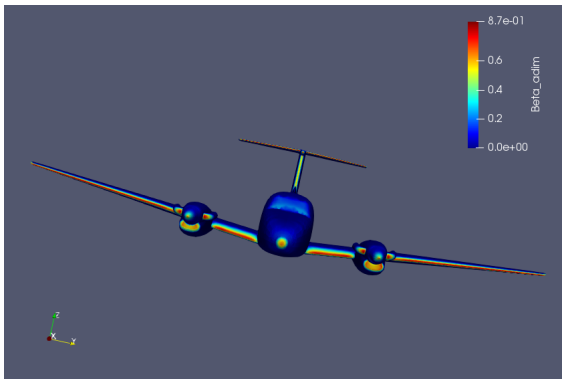

Figure 12: Local collection efficiency on a turboprop aircraft, $d = 60\mu m$, Mach=0.2, AoA=0^o

Finally, the droplet solution is compute (figure 12) on a turboprop aircraft with the same method at Mach 0.2 at a 0° angle of attack and with an Euler air flow. In this simplified model, the propellers are not modelled. The areas of high impingement intensity are concentrated on the nose, the airfoil edges and the stabilizer of the plane. Those are the areas that usually need ice protection systems on a turboprop aircraft [11]. This last test case shows the possibility of using this solver on a complex 3D geometry.

4 Conclusion

In this work, a development and implementation of a positivity-preserving scheme for the Eulerian formulation of the droplet equations is proposed in the context of aircraft icing. Numerical results within SU2 are in agreement with the literature and underscore the good scheme properties especially in low density areas where the density remains positive on every test cases. Because of the low local collection efficiency sensitivity to spacial discretization, satisfactory results can be achieved with relatively coarse meshes. The use of the Euler equations to compute the airflow is certainly an approximation in this study but its impact remains uncertain at low angles of attack. Future work could consider the use of a Navier-Stokes based air flow and the required adjustments to the boundary condition treatment in order to take the boundary layer into account.

References

[1] I.A.T.A., Safety Report 2015. *International Air Transport Association: Montreal*, Quebec, (2016).

[2] Bragg, M.B., Broeren, A.P., and Blumenthal, L.A., Iced-airfoil aerodynamics. *Progress in Aerospace Sciences 2005*, 41, No. 5, (2005), p. 323-362.

[3] Yves Bourgault, Wagdi G. Habashi, Julien Dompierre and Guido S. Baruzzi A finite element method study of eulerian droplets impingement models *Int. J. Numer Meth. Fluids*, 29, (1999), p. 429-449.

[4] Economon, T.D., Palacios, F., Copeland, S.R., Lukaczyk, T.W., and Alonso, J.J., SU2: An Open-Source Suite for Multiphysics Simulation and Design. *AIAA Journal 2015*, 54, No. 3, (2015), p. 828-846.

[5] S.K. Jung, R.S. Myong. A second-order positivity-preserving finite volume upwind scheme for air-mixed droplet flow in atmospheric icing. *Comput Fluids 86 (2013)*, p. 459-469.

[6] E.F. Toro. Riemann Solvers and Numerical Methods for Fluid Dynamics. *Springer (2009)*.

[7] P. Batten, M. A. Leschziner, dU. C. Goldberg. Average-State Jacobians and Implicit Methods for Compressible Viscous and Turbulent Flows. *J Comput Phys 137 (1997)*, p. 38-78.

[8] Naveen Kumar Garg, Michael Junk, S.V. Raghurama Rao, M. Sekhar. An upwind method for genuine weakly hyperbolic systems. *arXiv:1703.08751* (2017).

[9] J. Blazek. Computational Fluid Dynamics: Principles and Applications. *Third Edition, Elsevier Ltd (2015)*.

[10] M. Papadakis, K. Hung, Giao T. Vu, Hsiung-Wei Yeong, C. Bidwell, M. D. Breer and T. Bencic. Experimental Investigation of Water Droplet Impingement on Airfoils, Finite Wings, and an S-duct Engine Inlet. (2002).

[11] Bowden, D.T., Gensemer, A.E., and Speen. Engineering Summary of Airframe Icing Technical Data. Federal Aviation Agency (1963).